Co-published by
Institute of Fluid-Flow Machinery
Polish Academy of Sciences
Committee on Thermodynamics and Combustion
Polish Academy of Sciences

http://www.imp.gda.pl/archives-of-thermodynamics/

Hybrid nanofluid past time-dependent radially stretched sheet with Dufour and Soret effects

D. Srinivasacharya[a*], M. V. Sreekantha Reddy[b]

[a]Department of Mathematics, National Institute of Technology, Telangana, India
[b]Gokaraju Rangaraju Institute of Engineering and Technology, Bachupally, Hyderabad, 500090, India
*Corresponding author email: dsc@nitw.ac.in

Received: 11.12.2024; revised: 01.08.2025; accepted: 03.08.2025

Abstract

The steady laminar flow past a time-dependent radially stretching sheet with Soret and Dufour effects within a hybrid nanofluid is studied. The governing equations are transformed into ordinary differential equations utilising the similarity transformations. Successive linearization is employed to linearise the nonlinear system of equations. The resultant system of equations is solved using the Chebyshev collocation method. Plots of the velocity, temperature, and concentration for chosen parameters are displayed in conjunction with the Sherwood number, Nusselt number, and coefficient of skin friction. As the volume fraction of copper (Cu) nanoparticles increases, the important values of these variables decrease, while increasing the amount of alumina (Al_2O_3) nanoparticles causes them to rise. The hybrid nanofluid demonstrates a faster heat transfer rate than the nanofluid on the radially stretched surface. Additionally, it has been discovered that increasing the volume fractions of copper (Cu) nanoparticles minimizes the coefficient of skin friction, the Sherwood number, and the Nusselt number for the stretching surface, while increasing the volume fractions of alumina (Al_2O_3) nanoparticles boosts the skin friction coefficient, the Sherwood number, and lowers the Nusselt number. Furthermore, increasing the Dufour number maintains the Sherwood number at a constant level while decreasing the Nusselt number; in contrast, enhancing the Soret number decreases the Sherwood number and increases the Nusselt number.

Keywords: Hybrid nanofluid; Radially stretching sheet; Successive linearisation method; Dufour and Soret effects

Vol. 46(2025), No. 4, 19–30; doi: 10.24425/ather.2025.156595

Cite this manuscript as: Srinivasacharya, D., & Sreekantha Reddy, M.V. (2025). Hybrid nanofluid past time-dependent radially stretched sheet with Dufour and Soret effects. *Archives of Thermodynamics*, 46(4), 19−30.

1. Introduction

Fluid flow across a sheet that is stretched radially is a significant subject in chemical, metallurgical, and biological engineering applications. It also plays a key role in wire drawing, hot rolling, polymer extrusion, metal spinning, and liquid metal processing. Numerous researchers have examined the features of mass and heat transmission in Newtonian and non-Newtonian fluid flow. Khan et al. [1] addressed the heat transfer and axisymmetric flow of a cross fluid on a radially stretched sheet. Ahmed et al. [2] investigated the effects of radiation and an angled magnetic field on the Sisko fluid across a sheet that is stretched radially. Utilising the homotopy analysis approach, Sreelakshmi et al. [3] explored the time-dependent Jeffrey nanofluid flow across a surface that is expanding radially by employing convective boundary conditions. Khan et al. [4] investigated the flow across a stretched sheet involving several slips, radiation, chemical reactions, and magnetic impacts. Nayak et al. [5] evaluated the

Nomenclature

A – unsteadiness parameter, (c/a)
a, b, c, d (≥ 0) – constants
$C(r, z, t)$ – concentration, mol
C_∞ – concentration of the surrounding medium, mol
C_f – coefficient of skin friction
C_p – specific heat at constant pressure, J/(kg K)
C_s – concentration susceptibility of the hybrid nanofluid
C_w ($C_w > C_\infty$) – concentration at the stretched surface, mol
Df – Dufour number $\left(\frac{D_m K_t (C_w - C_\infty)}{C_s C_p \nu (T_w - T_\infty)}\right)$
D_m – mass diffusivity, (m^2/s)
$f'(\eta)$ – dimensionless velocity
K_T – thermal diffusion ratio, 1/K
k_{hnf} – thermal conductivity of the hybrid nanofluid, W/(m K)
Nu – Nusselt number
Pr – Prandtl number, (ν/α_f)
r, z – radial and axial coordinate axes, m
Re – local Reynolds number, (rU_w/ν)
Sh – Sherwood number
Sc – Schmidt number (ν/D_m)
Sr – Soret number $\left(\frac{D_m K_t (T_w - T_\infty)}{T_m \nu (C_w - C_\infty)}\right)$
T_∞ ($T_w > T_\infty$) – temperature of the surrounding medium, K
$T(r, z, t)$ – temperature, K
T_m – mean fluid temperature, K
T_w – temperature at the stretched surface, K
$u(r, z, t)$, $w(r, z, t)$ – velocity components in r and z direction, m/s
U_w – time-dependent stretching velocity, m/s
W_0 – suction/injection velocity

Greek symbols

α – thermal diffusivity, m^2/s
μ – dynamic viscosity, Pa·s
ν – kinematic viscosity, m^2/s
ρ – density, kg/m^3
$\psi(r, z)$ – stream function

Subscripts and Superscripts

$n1$ – for the Al_2O_3 nanoparticles
$n2$ – for the Cu nanoparticles
f – for the fluid
hnf – for hybrid nanofluid

Abbreviations and Acronyms

CNT – carbon nanotube
MHD – magnetohydrodynamics
SLM – successive linearisation method

influence of a chemical reaction on mass transfer flow across a radially elongated sheet. The majority of research on the radially expanded surface focuses on steady-state conditions. On the other hand, unsteadiness becomes a crucial subject of analysis in many engineering processes. Shahzad et al. [6,7] analysed the effect of axially symmetrical flow and heat exchange on a time dependent radially stretching surface. Srinivasacharya and Shravan Kumar [8] used artificial neural networks to investigate the movement of Casson fluid across an unsteady sheet that is expanding radially under Soret and Dufour's influence.

Further, simultaneous heat and mass transfer from different geometries embedded in porous media has many engineering and geophysical applications. Chamkha and Khaled [9] considered simultaneous heat and mass transfer of an electrically-conducting fluid by mixed convection in a stagnation flow over a flat plate embedded in a porous medium in the presence of wall blowing or suction, magnetic field effects, and temperature-dependent heat generation or absorption effects. Krishna et al. [10] studied the effects of heat and mass transfer on free convective flow of micropolar fluid over an infinite vertical porous plate in the presence of an inclined magnetic field with a constant suction velocity and taking Hall current into account. Krishna et al. [11] explored the Hall and ion slip impacts on an unsteady laminar magnetohydrodynamics (MHD) convective rotating flow of heat generating or absorbing second grade fluid over a semi-infinite vertical moving permeable surface.

The topic of heat transfer improvement has gained lots of attention in the last several years. Since nanoparticles have a higher thermal conductivity than base fluid, thermal scientists have proposed including metallic or non-metallic nanoparticles in the base fluid to boost its thermal conductivity. A nanofluid is the resultant blend with enhanced chemical and physical characteristics. In 1995, Choi and Eastman [12] coined the term "nanofluid." However, to accelerate heat transmission, researchers are looking into hybrid nanofluids, a new kind of nanofluids. Ordinary nanofluid contains only one nanoparticle in the base fluid, whereas hybrid nanofluid is considered a superior nanofluid, consisting of two distinct nanoparticles. Hybrid nanofluid provides better thermophysical qualities, thereby enhancing heat transfer efficiency. Other than the atypically high effective thermal conductivity, hybrid nanofluid can provide great benefits when the nanosized particles are adequately dispersed. Hybrid nanofluid has been introduced to investigate the properties of heat transfer and make it even better. Heat transfer in the fields of microelectronics, microfluidics, manufacturing, and medicine are a few of the applications for hybrid nanofluids. Several researchers have analysed the heat transfer and boundary layer flow of hybrid nanofluids. Devi and Devi [13,14] examined Cu nanoparticles regardless of magnetic effects when studying the motion of a hybrid nanofluid across a stretched surface. They discovered that, compared to ordinary nanofluid, hybrid nanofluid increases the heat transmission rate. Recently, many researchers, including Hayat and Nadeem [15], Yousefi et al. [16], Subhani and Nadeem [17], Ghadikolaei et al. [18], Usman et al. [19], Rostami et al. [20], and Waini et al. [21,22] have analysed the heat and mass transfer properties in a hybrid nanofluid flow.

Gangadhar et al. [23] studied the impact of convective heating boundary on a second-grade nanofluid flow alongside a Riga pattern using a Grinberg term and a Lorentz force applied parallel to the wall of the Riga plate. Ontela et al. [24] studied the behaviour of a conducting hybrid nanofluid comprised of CuO and Cu nanoparticles over a nonlinear stretching surface filled with a porous matrix. Panda et al. [25] investigated the optimisation of heat transportation rate in a nonlinear radiative buoyancy-driven hydromagnetic carbon nanotube (CNT) hybrid nanofluid flow.

Pattnaik et al. [26] analysed the convective transport of radiative blood flow properties in the context of a heated stretch-

ing/shrinking conducting Riga sensor plate. Panda et al. [27] considered the influence of radiating heat on the flow of Powell-Eyring fluid over a Riga plate subjected to thermal stratification, utilising the Cattaneo-Christov heat flux model.

The Dufour and Soret effects in hybrid nanofluids have been the subject of extensive research in recent years. Mass and heat transmission in a fluid flow are referred to as Dufour and Soret effects. In addition to mass transfer (the Soret effect), the temperature gradient produces variations in concentration. These two effects, Dufour and Soret, are simultaneous coupling processes. Nisar et al. [28] studied the effects of Dufour and Soret in the flow of hybrid nanofluids using numerical methods. Abad et al. [29] have documented their exploration of the implications of the stagnation point on a hybrid nanofluid based on water, in which alumina and Cu are the nanoparticles. Hayat et al. [30] examined the consequences of Soret and Dufour numbers on the magnetohydrodynamic movement of the Casson fluid across an extended surface. Kameswaran et al. [31] addressed the stagnation point flow of a Casson fluid along a stretched sheet in the presence of Dufour and Soret effects.

Many investigators have analysed the Soret and Dufour effects on the flow of hybrid nanofluid in various geometries. Isa et al. [32] researched the consequence of the Soret and Dufour effects on the flow of a hybrid nanofluid made of copper and alumina nanoparticles in water. Prathiba et al. [33] explored the Soret and Dufour effects over a rotating hybrid nanofluid. In the context of Dufour and Soret effects, Arif et al. [34] assessed numerically the simultaneous transmission of mass and heat in a Maxwell hybrid nanofluid. Sharma et al. [35] performed a comparative analysis of the Ag-CuO/H_2O hybrid nanofluid flow across an inclined stretched surface incorporating Dufour and Soret effects. Vijay et al. [36] evaluated magnetohydrodynamic hybrid nanofluid flow on a revolving, slowing-down disk using Dufour and Soret effects.

From the available literature, the flow of hybrid nanofluid over radially shrinking and stretching sheets is extremely rare, and none of the published articles consider separately the effect of Dufour and Soret parameters on such a fluid stream. Most of the investigations on the radially stretching sheet are restricted to steady-state. However, when the flow depends on time, unsteadiness becomes an important component of study in a variety of engineering processes, e.g. in solar energy, refrigeration, heating, ventilation, and air conditioning applications. Hence, to bridge the gap, this paper investigates the hybrid nanofluid flow behaviour and heat transmission across the time-dependent radially extending surface with Soret and Dufour effects utilising the Tiwari and Das nanofluid model. Hybrid nanofluid is generated by suspending alumina and Cu nanoparticles in water.

In the present study, the aluminium and copper nanoparticles are chosen because of their unique thermal properties. The combination of aluminium oxide and copper helps to maintain nanofluid consistency over time while also giving strong thermal characteristics. $Cu - Al_2O_3$: H_2O is one of the attractive choices for improved heat transfer in industries like electronics cooling, power generation, and chemical processing. As copper is one of the most thermally conductive metals, it enhances the thermal conductivity significantly, and Al_2O_3 adds stability and strength. The data of the current analysis is compared with the numerical results to verify the findings.

2. Problem formulation

The unsteady and laminar flow of a hybrid nanofluid over a radially stretching surface with Soret and Dufour effects is considered here. Figure 1 depicts the coordinate system and geometry. The flow is a consequence of the radial stretching of the surface, which has a time-dependent velocity: $U_w = ar/(1-ct)$. Let $C_w = C_\infty + dr/(1-ct)$ and $T_w = T_\infty + br/(1-ct)$ indicate the concentration and the temperature at the stretched surface, respectively. Here, C_∞ ($C_w > C_\infty$) and T_∞ ($T_w > T_\infty$) are the concentration and temperature of the surrounding medium, with $ct < 1$ and a, b, c, d (≥ 0) are constants. ∞

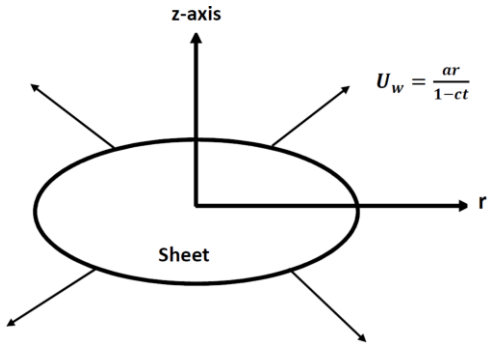

Fig. 1. Coordinate system and geometry.

The equations that govern the flow are [37–39]:

$$\frac{\partial u}{\partial r} + \frac{u}{r} + \frac{\partial w}{\partial z} = 0, \tag{1}$$

$$\frac{\partial u}{\partial t} + u\frac{\partial u}{\partial r} + w\frac{\partial u}{\partial z} = \frac{\mu_{nnf}}{\rho_{nnf}}\frac{\partial^2 u}{\partial z^2}, \tag{2}$$

$$\frac{\partial T}{\partial t} + u\frac{\partial T}{\partial r} + w\frac{\partial T}{\partial z} = \frac{K_{nnf}}{(\rho C_P)_{nnf}}\frac{\partial^2 T}{\partial z^2} + \frac{D_m K_T}{C_S C_P}\frac{\partial^2 C}{\partial z^2}, \tag{3}$$

$$\frac{\partial C}{\partial t} + u\frac{\partial C}{\partial r} + w\frac{\partial C}{\partial z} = D_m\frac{\partial^2 C}{\partial z^2} + \frac{D_m K_T}{T_m}\frac{\partial^2 T}{\partial z^2}. \tag{4}$$

Following Devi and Devi [13,14], and Oztop and Abu-Nada [40], fluid and hybrid nanofluid thermophysical properties are assessed using the equations demonstrated in Table 1.

Table 1. Thermophysical characteristics of hybrid nanofluid and fluid.

Property	Fluid	Hybrid nanofluid [13,14,40]
Heat capacity	$(\rho C_p)_f$	$(\rho C_p)_{hnf} = (1-\phi_2)\times \left[(1-\phi_1)(\rho C_p)_f + \phi_1(\rho C_p)_{n1}\right] + \phi_2(\rho C_p)_{n2}$
Dynamic viscosity	μ_f	$\mu_{hnf} = \left[\frac{\mu_f}{((1-\phi_1)(1-\phi_2))^{2.5}}\right]$
Density	ρ_f	$\rho_{hnf} = \phi_2\rho_{n2} + (1-\phi_2)\left[(1-\phi_1)\rho_f + \phi_1\rho_{n1}\right]$
Thermal conductivity	k_f	$\frac{k_{hnf}}{k_{nf}} = \left[\frac{k_{n2} - 2\phi_2(k_{nf} - k_{n2} + 2k_{nf})}{k_{n2} + \phi_2(k_{nf} - k_{n2}) + 2k_{nf}}\right]$ where: $\frac{k_{nf}}{k_f} = \left[\frac{k_{n1} - 2\phi_1(k_f - k_{n1}) + 2k_f}{k_{n1} + \phi_1(k_f - k_{n1}) + 2k_f}\right]$

Table 2 gives the same information as Oztop and Abu-Nada [40] regarding the base fluid and nanoparticles. In this case, the subscripts $n1$, $n2$, f, and hnf stand for the Al_2O_3, Cu nanoparticles solid components, fluid, and hybrid nanofluid.

Table 2. Fluid thermophysical characteristics and nanoparticles [40].

Characteristics	Cu	Al_2O_3	Water
k, W/(m K)	400	40	0.613
C_p, J/(kg K)	385	765	4179
ρ, kg/m^3	8933	3970	997.1

The boundary conditions on the surface are:

$$w = W_0, \quad u = U_w = \frac{ra}{1-tc}, \quad T_w = T_\infty + \frac{rb}{1-tc},$$
$$C_w = C_\infty + \frac{rd}{1-tc} atz = 0, \tag{5}$$
$$u \to 0, \quad C \to C_\infty, \quad T \to T_\infty asz \to \infty,$$

where U_w is the velocity of stretching and $W_0 = -2S\left[\frac{\nu U_w}{r}\right]^{\frac{1}{2}}$. Here on the surface, $W_0 < 0$ ($S > 0$) signifies suction and $W_0 > 0$ ($S < 0$) signifies injection.

The similarity transformations for the present problem are given by:

$$\psi(r,z) = -r^2 U_w \mathrm{Re}^{-1/2} f(\eta), \qquad \eta = \frac{z}{r}\mathrm{Re}^{1/2},$$
$$\theta = \frac{T-T_\infty}{T_w-T_\infty}, \qquad \phi(\eta) = \frac{C-C_\infty}{C_w-C_\infty}, \tag{6}$$

where $\psi(r,z)$ represents the stream function defined by $u = -\frac{1}{r}\frac{\partial\psi}{\partial z}$ and $w = \frac{1}{r}\frac{\partial\psi}{\partial r}$. $\mathrm{Re} = \frac{rU_w}{\nu}$ denotes the local Reynolds number.

Substituting Eq. (6) into Eqs. (1)–(4), leads to the dimensionless equations shown below:

$$\left[\frac{\mu_{hnf}\rho_f}{\rho_{hnf}\mu_f}\right] f''' + 2ff'' - f'^2 - A\left[\frac{1}{2}\eta f'' + f'\right] = 0, \tag{7}$$

$$\left[\frac{1}{\mathrm{Pr}}\frac{K_{hnf}(\rho C_p)_f}{(\rho C_p)_{hnf}K_f}\right]\theta'' + \mathrm{Df}\cdot\phi'' + 2f\theta' + $$
$$-f'\theta - A\left[\frac{1}{2}\eta\theta' + \theta\right] = 0, \tag{8}$$

$$\mathrm{Sr}\cdot\theta'' + \frac{1}{S_c}\phi'' + 2f\phi' - f'\phi - A\left[\phi + \frac{1}{2}\eta\phi'\right] = 0. \tag{9}$$

The accompanying boundary conditions are changed to the subsequent form:
at $\eta = 0$:

$$\theta(0) = 1, \quad f'(0) = 1, \quad f(0) = S, \quad \phi(0) = 1, \tag{10a}$$

as $\eta \to \infty$:

$$\theta(\eta) \to 0, \qquad f'(\eta) \to 0, \qquad \phi(\eta) \to 0. \tag{10b}$$

The mass transfer rate (Sherwood number Sh), the heat transfer rate (Nusselt number Nu), and the coefficient of skin friction C_f are defined by:

$$\mathrm{Sh} = -\frac{r}{(C_w-C_\infty)}\left(\frac{\partial C}{\partial z}\right)_{z=0}, \qquad C_f = \frac{2}{\rho U_w^2}\mu\left(\frac{\partial u}{\partial z}\right)_{z=0},$$
$$\mathrm{Nu} = -\frac{r}{(T_w-T_\infty)}\left(\frac{\partial T}{\partial z}\right)_{z=0}. \tag{11}$$

The non-dimensional form of Sherwood number Sh, skin friction coefficient C_f, and Nusselt number Nu are:

$$\mathrm{Re}^{-\frac{1}{2}}\mathrm{Sh} = -\phi'(0), \qquad \frac{1}{2}\mathrm{Re}^{\frac{1}{2}}C_f = f''(0),$$
$$\mathrm{Re}^{-\frac{1}{2}}\mathrm{Nu} = -\theta'(0). \tag{12}$$

3. Method of solution

The basic principle of the successive linearisation method (SLM) is the assumption that the functions $f(\eta)$, $\theta(\eta)$ and $\phi(\eta)$ can be interpreted as:

$$f(\eta) = f_k(\eta) + \sum_{m=0}^{k-1} f_m(\eta),$$
$$\theta(\eta) = \theta_k(\eta) + \sum_{m=0}^{k-1} \theta_m(\eta), \tag{13}$$
$$\phi(\eta) = \phi_k(\eta) + \sum_{m=0}^{k-1} \phi_m(\eta).$$

Here, f_k, θ_k and ϕ_k (k = 1, 2, 3, …) are unknown functions and θ_m, f_m, and ϕ_m ($m \geq 1$) are the approximations that can be acquired repeatedly by computing the solution of the linear portion of the equations that arises from putting Eq. (13) into Eqs. (7)–(9). The basic principle concerning SLM is that when k grows in size, f_k, θ_k and ϕ_k become progressively smaller and thus ignored, i.e.

$$\lim_{k\to\infty} f_k = \lim_{k\to\infty} \theta_k = \lim_{k\to\infty} \varphi_k = 0. \tag{14}$$

The initial assumptions for $f_0(\eta)$, $\theta_0(\eta)$ and $\phi_0(\eta)$ are made to fulfil the boundary conditions. The differential equations for f_k, θ_k and ϕ_k ($k \geq 1$) are found by substituting Eq. (13) into Eqs. (7) – (9) and then taking only the linear terms.

$$a_1 f_k''' + a_2 f_k'' + a_3 f_k' + a_4 f_k = r_1, \tag{15}$$

$$b_1 f_k' + b_2 f_k + b_3\theta_k'' + b_4\theta_k' + b_5\theta_k + \mathrm{Df}\cdot\phi_k'' = r_2, \tag{16}$$

$$c_1 f_k' + c_2 f_k + \mathrm{Sr}\cdot\theta_k'' + \frac{1}{S_c}\phi_k'' + c_3\phi_k' + c_4\phi_k = r_3. \tag{17}$$

The linearised boundary conditions are:

$$\phi_k(0) = \phi_k(\infty) = 0,$$
$$f_k(0) = f_k'(0) = f_k'(\infty) = 0, \tag{18}$$
$$\theta_k(0) = \theta_k(\infty) = 0,$$

where the coefficients a_q (q = 1, 2, 3, 4), b_z (z = 1, 2, 3, 4, 5), c_n (n = 1, 2, 3, 4), and r_p (p = 1, 2, 3) are:

$$a_1 = \frac{\mu_{hnf}\rho_f}{\rho_{hnf}\mu_f}, \qquad a_2 = 2\sum_{m=0}^{k-1} f_m - \frac{A}{2}\eta,$$
$$a_3 = -[2\sum_{m=0}^{k-1} f_m' + A], \qquad a_4 = 2\sum_{m=0}^{k-1} f_m'',$$
$$r_1 = -a_1\sum_{m=0}^{k-1} f_m''' + \left[\frac{A}{2}\eta - 2\sum_{m=0}^{k-1} f_m\right]\sum_{m=0}^{k-1} f_m'' +$$
$$+(\sum_{m=0}^{k-1} f_m')^2 + A\sum_{m=0}^{k-1} f_m',$$

$$b_1 = -\sum_{m=0}^{k-1}\theta_m, \quad b_2 = 2\sum_{m=0}^{k-1}\theta'_m, \quad b_3 = \frac{1}{\Pr}\frac{K_{hnf}(\rho C_p)_f}{(\rho C_p)_{hnf}K_f},$$

$$b_4 = 2\sum_{m=0}^{k-1} f_m - \frac{A}{2}\eta, \qquad b_5 = -[A + \sum_{m=0}^{k-1} f'_m],$$

$$r_2 = -b_3\sum_{m=0}^{k-1}\theta''_m + \left[\frac{A}{2}\eta - 2\sum_{m=0}^{k-1} f_m\right]\sum_{m=0}^{k-1}\theta'_m + \\ +(\sum_{m=0}^{k-1} f'_m + A)\sum_{m=0}^{k-1}\theta_m - \mathrm{Df}\sum_{m=0}^{k-1}\phi''_m,$$

$$c_1 = -\sum_{m=0}^{k-1}\phi_m, \qquad c_2 = 2\sum_{m=0}^{k-1}\phi'_m, \quad ,$$

$$c_3 = 2\sum_{m=0}^{k-1} f_m - \frac{A}{2}, \qquad c_4 = -[A + \sum_{m=0}^{k-1} f'_m],$$

$$r_3 = -\frac{1}{S_c}\sum_{m=0}^{k-1}\phi''_m + \left[\frac{A}{2}\eta - 2\sum_{m=0}^{k-1} f_m\right]\sum_{m=0}^{k-1}\phi'_m + \\ +(\sum_{m=0}^{k-1} f'_m + A)\ \sum_{m=0}^{k-1}\phi_m - \mathrm{Sr}\sum_{m=0}^{k-1}\theta''_m.$$

After calculating each solution for f_k, ϕ_k and θ_k (k ≥ 1) by repeatedly solving Eqs. (15)–(18) the following are the approximate values for $f(\eta)$, $\phi(\eta)$ and $\theta(\eta)$:

$$f(\eta) \approx \sum_{s=0}^{S} f_s(\eta),$$
$$\phi(\eta) \approx \sum_{s=0}^{S} \phi_s(\eta), \qquad (19)$$
$$\theta(\eta) \approx \sum_{s=0}^{S} \theta_s(\eta),$$

where S signifies the SLM approximation order.

The solution to the system of Eqs. (15)–(16) may be computed analytically (if possible) or numerically using any methods, most notably collocation methods, finite differences, shooting technique based on Runge-Kutta, and finite elements. This study uses the spectral collocation method using Chebyshev polynomials. This technique is based on using the Chebyshev interpolating polynomials to approximate the unknown functions in a way that allows them to collocate at the Gauss-Lobatto points:

$$\xi_k = \cos\frac{\pi k}{M}, \qquad k = 0,1,\dots,M, \qquad (20)$$

where M + 1 collocation points are utilised. To put the method into practice, the domain truncation technique is used to change the physical domain into the domain [0,L]. The domain is changed to [−1,1] using the following mapping:

$$\frac{\eta}{L} = \frac{\xi+1}{2}, \qquad -1 \le \xi \le 1, \qquad (21)$$

where L stands for the scaling value at infinity that activates the boundary condition. At the collocation points, the undefined functions f_k, θ_k and ϕ_k are approximated by the Chebyshev interpolating polynomials:

$$f_k(\xi) \approx \sum_{n=0}^{M} f_k(\xi_n) T_n(\xi_k),$$
$$\theta_k(\xi) \approx \sum_{n=0}^{M} \theta_k(\xi_n) T_n(\xi_k), \qquad (22)$$
$$\phi_k(\xi) \approx \sum_{n=0}^{M} \phi_k(\xi_n) T_n(\xi_k),$$

where k = 0, 1, 2, ..., M and T_n is the n^{th} Chebyshev polynomial described as:

$$T_n(\xi) = cos[n\cos^{-1}(\xi)]. \qquad (23)$$

The unknown function derivatives are computed as:

$$\frac{d^a f_k}{d\eta^a} = \sum_{n=0}^{M} D_{nj}^a f_k(\xi_n),$$
$$\frac{d^a \theta_k}{d\eta^a} = \sum_{n=0}^{M} D_{nj}^a \theta_k(\xi_n), \qquad (24)$$
$$\frac{d^a \phi_k}{d\eta^a} = \sum_{n=0}^{M} D_{nj}^a \phi_k(\xi_n),$$

where j = 0, 1, 2, …, M. Here $\mathbf{D}$ = 2D/L, where D is the Chebyshev spectral differentiation matrix and a is the order of differentiation. The matrix equation that emerges from substituting Eqs. (21)–(24) in Eqs. (15)–(18) is as follows.

$$\boldsymbol{B_{k-1}} X_k = Z_{k-1}, \qquad (25)$$

along with the conditions on the boundary:

$$f_k(\xi_M) = \sum_{n=0}^{M} D_{0n} f_k(\xi_n) = \sum_{n=0}^{M} D_{Nn} f_k(\xi_n) = 0,$$
$$\theta_k(\xi_M) = \theta_k(\xi_0) = \phi_k(\xi_M) = \phi_k(\xi_0) = 0, \qquad (26)$$

in which $\boldsymbol{B_{k-1}}$ is a square matrix of order 3(M + 1) and X_k $\boldsymbol{B_{k-1}}$ are column vectors 3(M + 1) × 1 described by:

$$B_{k-1} = \begin{bmatrix} B_{11} & B_{12} & B_{13} \\ B_{21} & B_{22} & B_{23} \\ B_{31} & B_{32} & B_{33} \end{bmatrix}, \quad X_k = \begin{bmatrix} F_k \\ \Theta_k \\ \Phi_k \end{bmatrix}, \quad Z_{k-1} = \begin{bmatrix} z_1 \\ z_2 \\ z_3 \end{bmatrix}, \qquad (27)$$

where:

$$B_{11} = a_1 D^3 + a_2 D^2 + a_3 D + a_4, \quad B_{12} = 0, \quad B_{13} = 0,$$
$$B_{21} = b_1 D + b_2, \quad B_{22} = b_3 D^2 + b_4 D + b_5, \quad B_{23} = \mathrm{Df}\cdot D^2,$$
$$B_{31} = c_1 D + c_2, \quad B_{32} = \mathrm{Sr}\cdot D^2, \quad B_{33} = \frac{1}{\mathrm{Sc}} D^2 + c_3 D + c_4,$$
$$F_k = [f_k(\xi_0), f_k(\xi_1), \dots, f_k(\xi_{M-1}), f_k(\xi_M)]^T,$$
$$\Theta_k = [\theta_k(\xi_0), \theta_k(\xi_1), \dots, \theta_k(\xi_{M-1}), \theta_k(\xi_M)]^T,$$
$$\Phi_k = [\phi_k(\xi_0), \phi_k(\xi_1), \dots, \phi_k(\xi_{M-1}), \phi_k(\xi_M)]^T,$$
$$z_1 = [r_1(\xi_0), r_1(\xi_1), \dots, r_1(\xi_{M-1}), r_1(\xi_M)]^T,$$
$$z_2 = [r_2(\xi_0), r_2(\xi_1), \dots, r_2(\xi_{M-1}), r_2(\xi_M)]^T,$$
$$z_3 = [r_3(\xi_0), r_3(\xi_1), \dots, r_3(\xi_{M-1}), r_3(\xi_M)]^T,$$
$$a_f\ (f = 2,3,4), \quad b_m\ (m = 1,2,4,5), \quad c_n\ (n = 1,2,3,4),$$

defined above are diagonal matrices of dimension (M + 1), and the transpose is indicated by the superscript T. On Eq. (25), the boundary constraints (26) are applied by altering the first and last rows of B_{mn} (m = 1, 2, 3; n = 1, 2, 3) and z_p (p = 1, 2, 3).

4. Findings and discussion

In the current investigation, the Sherwood number Sh, velocity, Nusselt number Nu, temperature, coefficient of skin friction C_f, and concentration are evaluated for distinct values of solid volume fraction of ϕ_1 (Al_2O_3), ϕ_2 (Cu), unsteadiness parameter A, Schmidt number Sc, suction/ injection parameter S, Soret number Sr, and Dufour number Df and are graphically represented. Unless otherwise stated, numerical computations are performed using ϕ_1 = 0.1, ϕ_2 = 0.1, A = 0.5, S = 0.5, Df = 0.5, Sc = 0.2 and Sr = 0.2 to assess the influence of all the parameters involved. Eqs. (7)–(9) are linearised using the successive linearisation procedure, and then the system is resolved by applying

the collocation technique. The resultant skin friction coefficient and Nusselt number are compared with the findings of previous investigations for $\phi_1 = \phi_2 = 0$. A well-justified comparison between our results and those of for $\theta'(0)$ and $f''(0)$ is demonstrated in Table 3.

Table 3. Comparison between $f''(0)$ and $\theta'(0)$ values at the surface by the current strategy with Shahzad et al. [6].

A	S	Pr	$f''(0)$		$\Theta'(0)$	
			Current values	Shahzad et al. [6]	Current values	Shahzad et al. [6]
0.5	1	1	-2.6713727	-2.655999	-2.4191865	-2.655999
0.5	0.5	1	-1.9147295	-1.907999	-1.7474918	-1.907999
0.5	0	1	-1.3104137	-1.308999	-1.2096476	-1.308999
0.5	-0.5	1	-0.8867758	-0.887200	-0.8309926	-0.887200
0.5	-1	1	-0.6192663	-0.620400	-0.5899393	-0.620400
0	0.5	1	-1.8041331	-1.798999	-1.6397280	-1.798999
0.5	0.5	0.5	-1.9147295	-1.907999	-1.0313962	-1.119999
0.5	0.5	0.7	-1.9147295	-1.907999	-1.3312163	-1.450000
1	0.5	1	-2.0244687	-2.016999	-1.8528471	-2.016999

Figure 2 demonstrates the influence of unsteadiness variable A over the velocity, heat transfer rate $-\theta'(0)$, temperature, and mass transfer rate, $-\phi'(0)$, concentration, and coefficient of skin friction $f''(0)$. An enhancement in A decreases the $f''(0)$, as demonstrated in Fig. 2a. This is due to the development of the velocity boundary layer is caused solely on the stretching plate. Figure 2b and Fig. 2c demonstrate that $-\phi'(0)$ and $-\theta'(0)$ enhance when parameter A increases. Physically, it means that the temperature gradient at the surface increases as A increases, which implies an increase of the heat transfer rate at the surface. The rise in parameter A led to an initial decrease in velocity, but later to a slow increment in the velocity, depicted in Fig. 2d. It can be viewed from Fig. 2e and Fig. 2f that the rise in parameter A led to a decrease in concentration and temperature.

The impact of ϕ_1 on the heat transfer rate $-\theta'(0)$, concentration, coefficient of skin friction $f''(0)$, temperature, mass transfer rate $-\phi'(0)$, and velocity is described in Fig. 3. It has been noted that as ϕ_1 increases, the $f''(0)$ and $-\phi'(0)$ escalate, as demonstrated in Fig. 3a and Fig. 3c, and $-\theta'(0)$ diminishes, as depicted in Fig. 3b. It appears that the rise in parameter ϕ_1 the enhances temperature and velocity, as shown in Fig. 3d and Fig. 3e and decreases the concentration, as displayed in Fig. 3f.

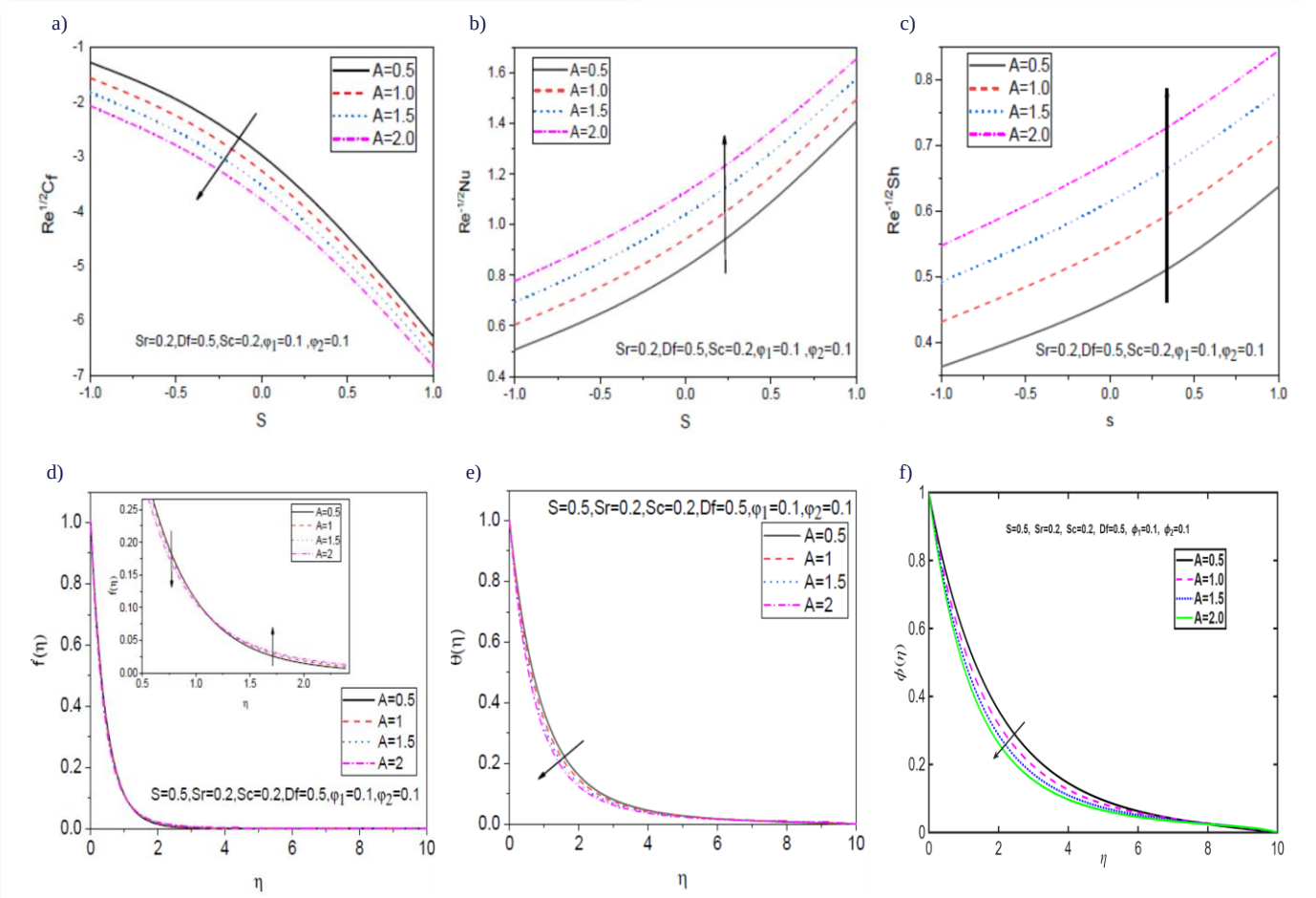

Fig. 2. Variation of $f''(0)$, $-\theta'(0)$, $-\phi'(0)$, $f'(\eta)$, $\theta(\eta)$ and $\phi(\eta)$ with unsteadiness parameter A.

The influence of ϕ_2 on velocity, skin friction coefficient $f''(0)$, temperature, mass transfer rate $-\phi'(0)$, concentration, and heat transfer rate $-\theta'(0)$, are shown in Fig. 4. As ϕ_2 increases, $f''(0)$, $-\theta'(0)$, and $-\phi'(0)$ reduce, depicted in Fig. 4a, Fig. 4b, and Fig. 4c. It is noticed that the boost in parameter ϕ_2 lowers velocity, as shown in Fig. 4d, but increases temperature and concentration as illustrated in Fig. 4e and Fig. 4f.

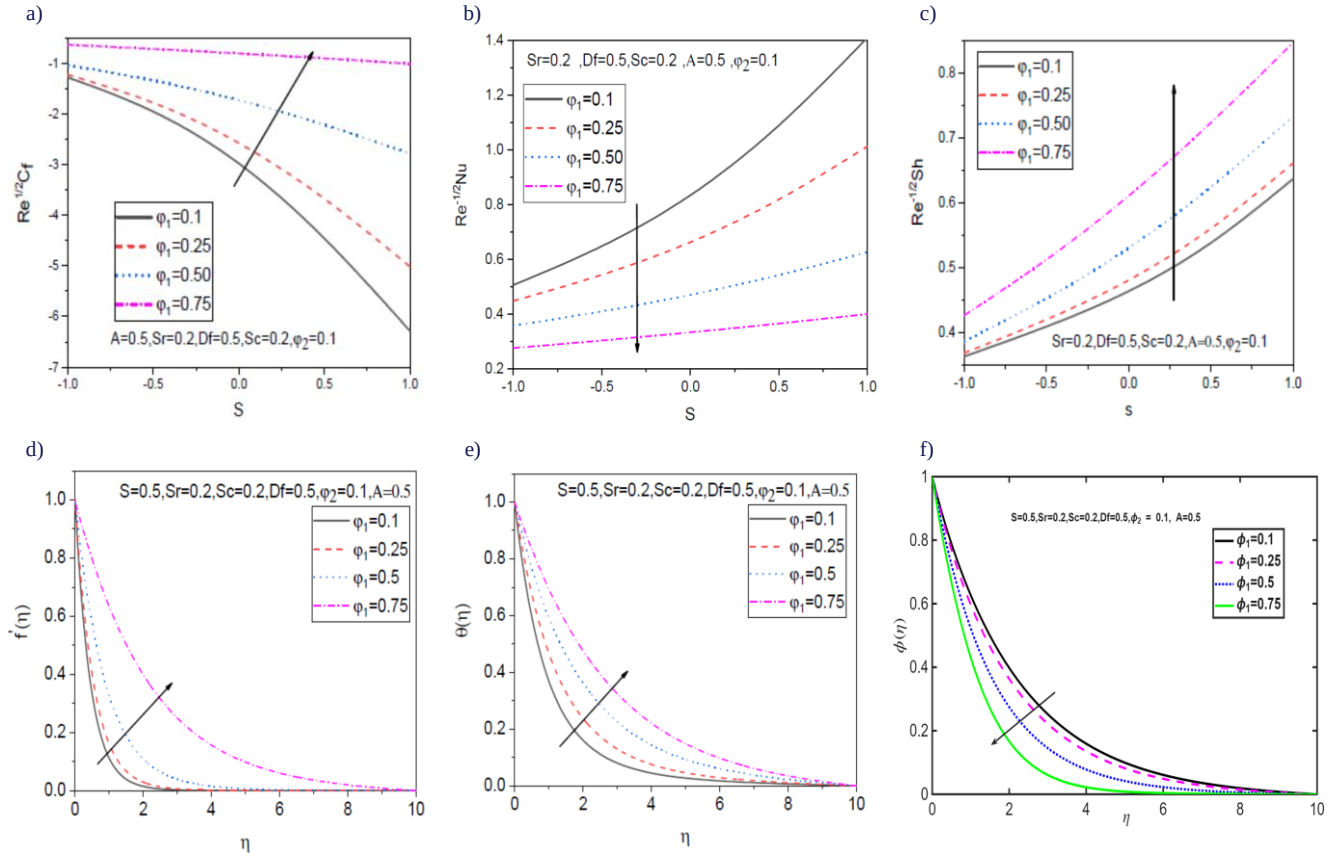

Fig. 3. Variation of $f''(0)$, $-\theta'(0)$, $-\phi'(0)$, $f'(\eta)$, $\theta(\eta)$ and $\phi(\eta)$ with nanoparticle volume fraction ϕ_1.

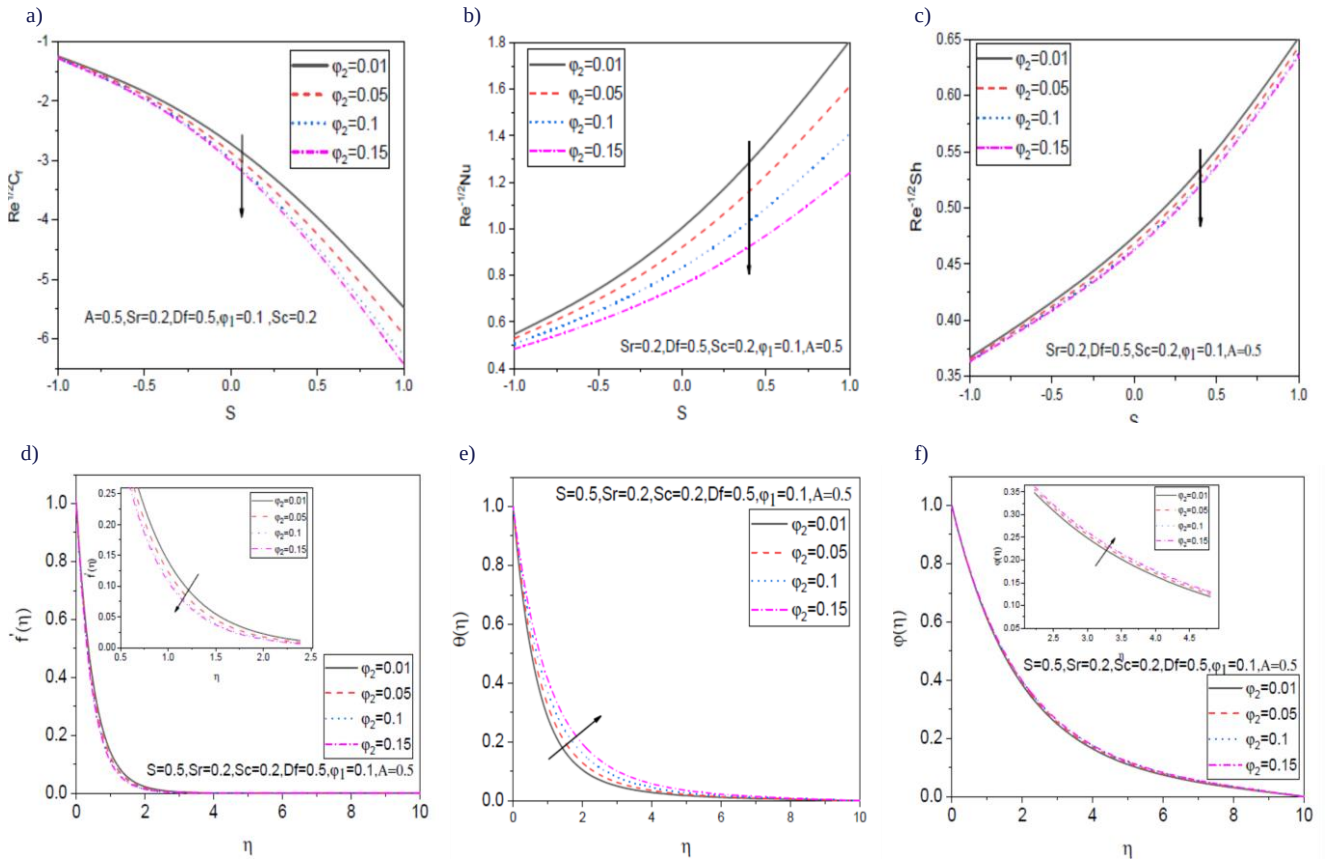

Fig. 4. Variation of $f''(0)$, $-\theta'(0)$, $-\phi'(0)$, $f'(\eta)$, $\theta(\eta)$ and $\phi(\eta)$ with nanoparticle volume fraction ϕ_2.

The impact of Schmidt number Sc on the velocity, mass transfer rate $-\phi'(0)$, concentration, heat transfer rate $-\theta'(0)$, temperature, and skin friction coefficient $f''(0)$ is demonstrated in Fig. 5. It has been noted that $f''(0)$, is unaffected by an increase in parameter Sc, as depicted in Fig. 5a. Figures 5b and 5c demonstrate that as Sc grows, $-\theta'(0)$ drops and $-\phi'(0)$ increases. It is noticed from Fig. 5d that the boost in parameter Sc does not affect velocity. Figure 5e demonstrates that as Sc enhances, the temperature initially increases and later diminishes. It is apparent from Fig. 5f that a spike in Sc reduces the concentration.

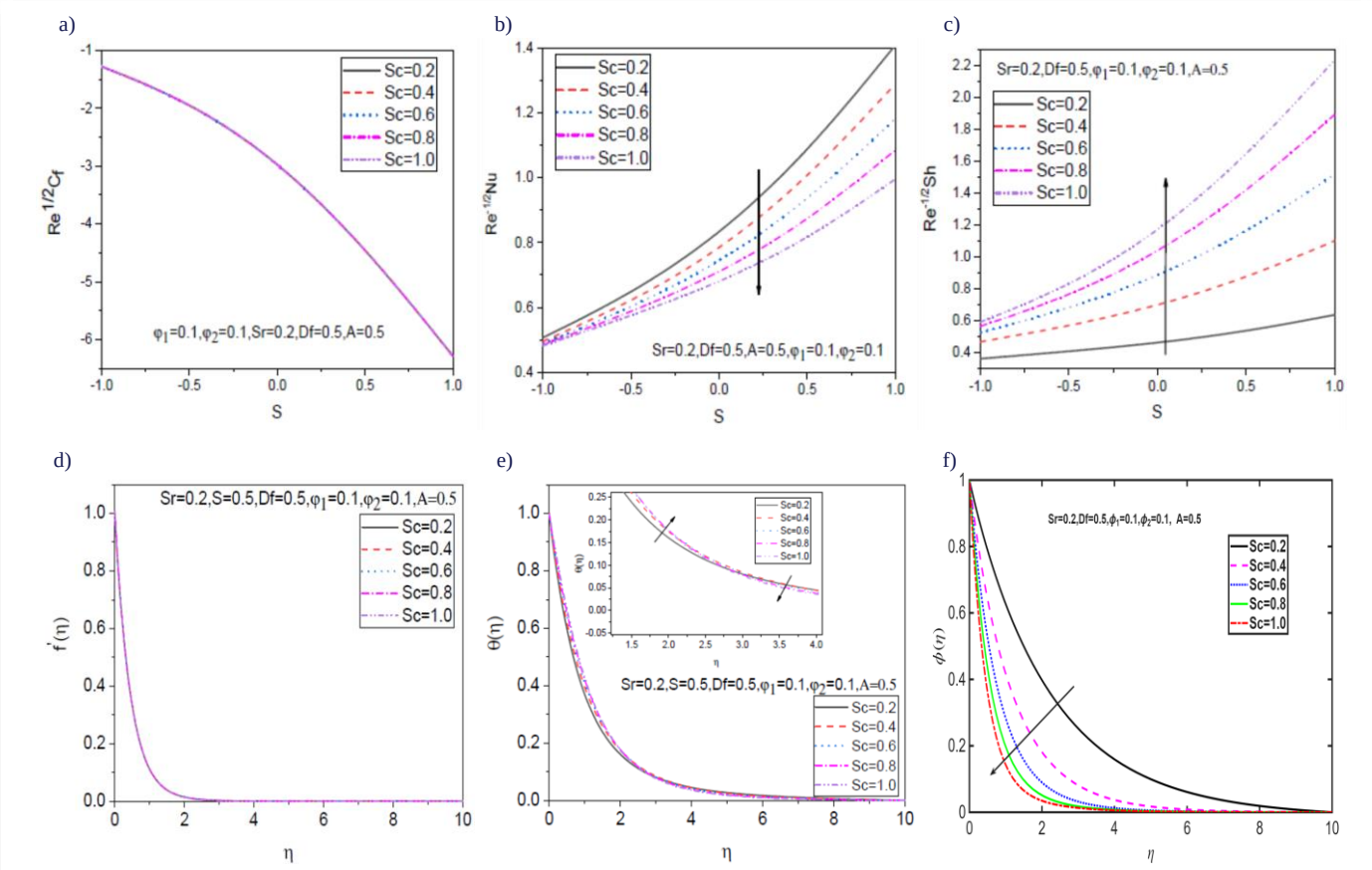

Fig. 5. Variation of $f''(0)$, $-\theta'(0)$, $-\phi'(0)$, $f'(\eta)$, $\theta(\eta)$ and $\phi(\eta)$ with Schmidt number Sc.

Figure 6 demonstrates the influence of the Soret number Sr over temperature and mass transfer rate $-\phi'(0)$, skin friction coefficient $f''(0)$, concentration, velocity, and heat transfer rate $-\theta'(0)$. The Soret number (Sr) describes the relative significance of mass diffusion (species diffusion) and thermal diffusion (heat conduction) in a fluid combination. When temperature gradients and concentration gradients combine, as they do in combustion, chemical processes, and in other reactive flow systems, the parameter Sr is especially important. It is noticed that as Sr increases, $f''(0)$ is constant and $-\theta'(0)$ escalates, as displayed in Fig. 6a and Fig. 6b. Figure 6c demonstrates that as Sr grows, $-\phi'(0)$ diminishes. Note that the rise in parameter Sr has no effect on velocity, but the temperature decreases, as shown in Fig. 6d and Fig. 6e. Figure 6f reveals that an increase in Sr increases concentration.

The enhancement in concentration is due to the Soret effect, where thermal gradients drive mass diffusion, enriching the species concentration near the surface. This enhanced diffusion also contributes to increased tangential motion. Conversely, the reduced temperature profile indicates that thermal energy is being redistributed to aid species transport, leading to a lower thermal boundary layer.

The influence of Dufour number Df on the heat transfer rate $-\theta'(0)$, coefficient of skin friction $f''(0)$, mass transfer rate $-\phi'(0)$, velocity, temperature, and concentration is presented in Fig. 7. The Dufour number Df describes how the diffusion coefficient in thermodynamics and transport phenomena changes with temperature $\theta(\eta)$. It reflects the temperature-dependent variation in the rate of diffusion and can be useful for understanding and simulating diffusion processes in a variety of systems, such as gases, liquids, and solids. Figure 7a depicts that the rise in the parameter Df does not influence the $f''(0)$. It is noticed from Fig. 7b and Fig. 7c that when the magnitude of the variable Df grows, $(-\theta')$ drops and $(-\phi')$ remains constant. The rise in parameter Df has no impact on velocity, but the increment in temperature is shown in Fig. 7d and Fig. 7e. This behaviour is attributed to the Dufour effect, where the energy flux induced by concentration gradients enhances thermal motion. It can be spotted from Fig. 7f that a spike in variable Df does not affect the concentration.

The outcome of the suction/injection parameter S on the concentration, velocity and temperature is apparent in Fig. 8. As the value of S rises, the temperature, velocity, and concentration diminish as presented in Figs. 8a, 8b and 8c.

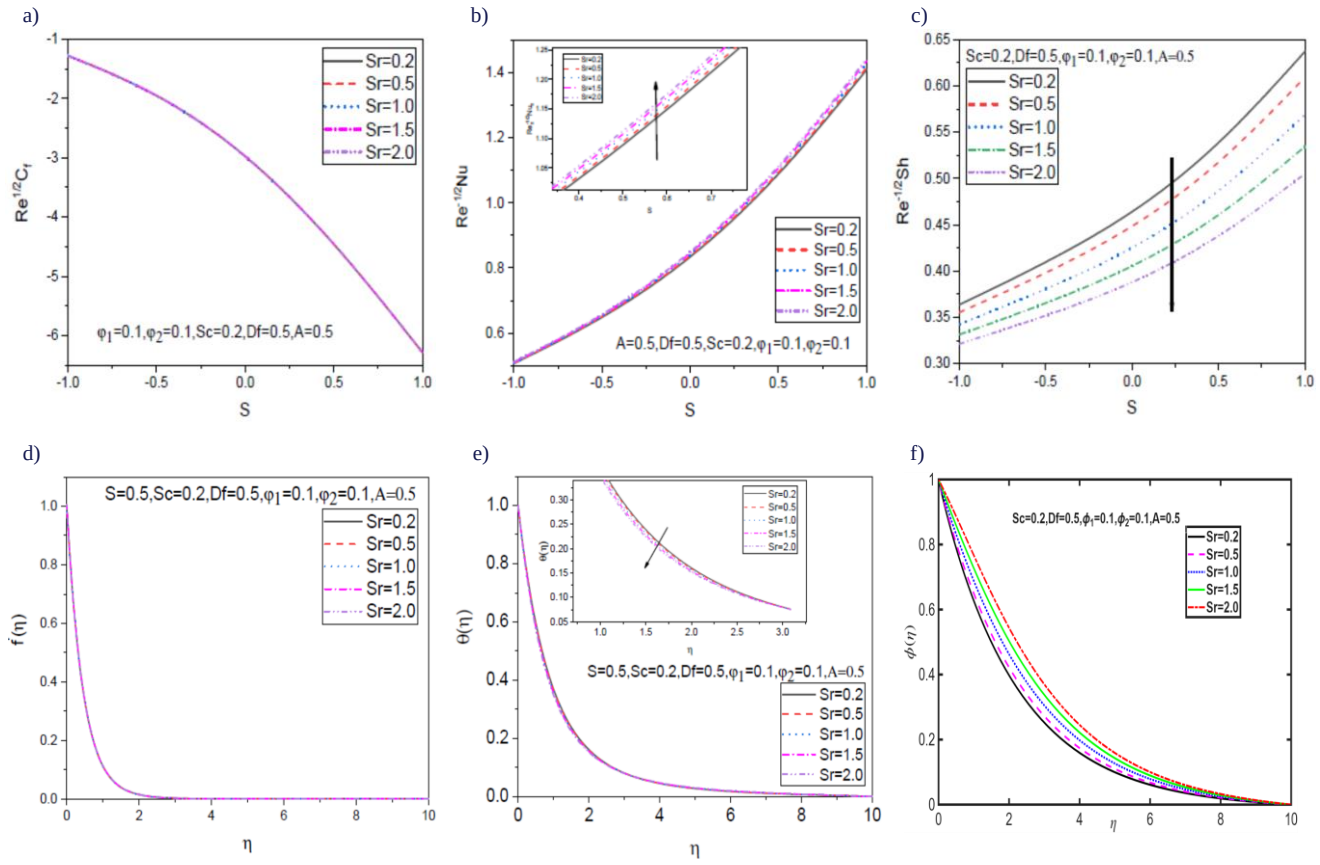

Fig. 6. Variation of $f''(0)$, $-\theta'(0)$, $-\phi'(0)$, $f'(\eta)$, $\theta(\eta)$ and $\phi(\eta)$ with Soret number Sr.

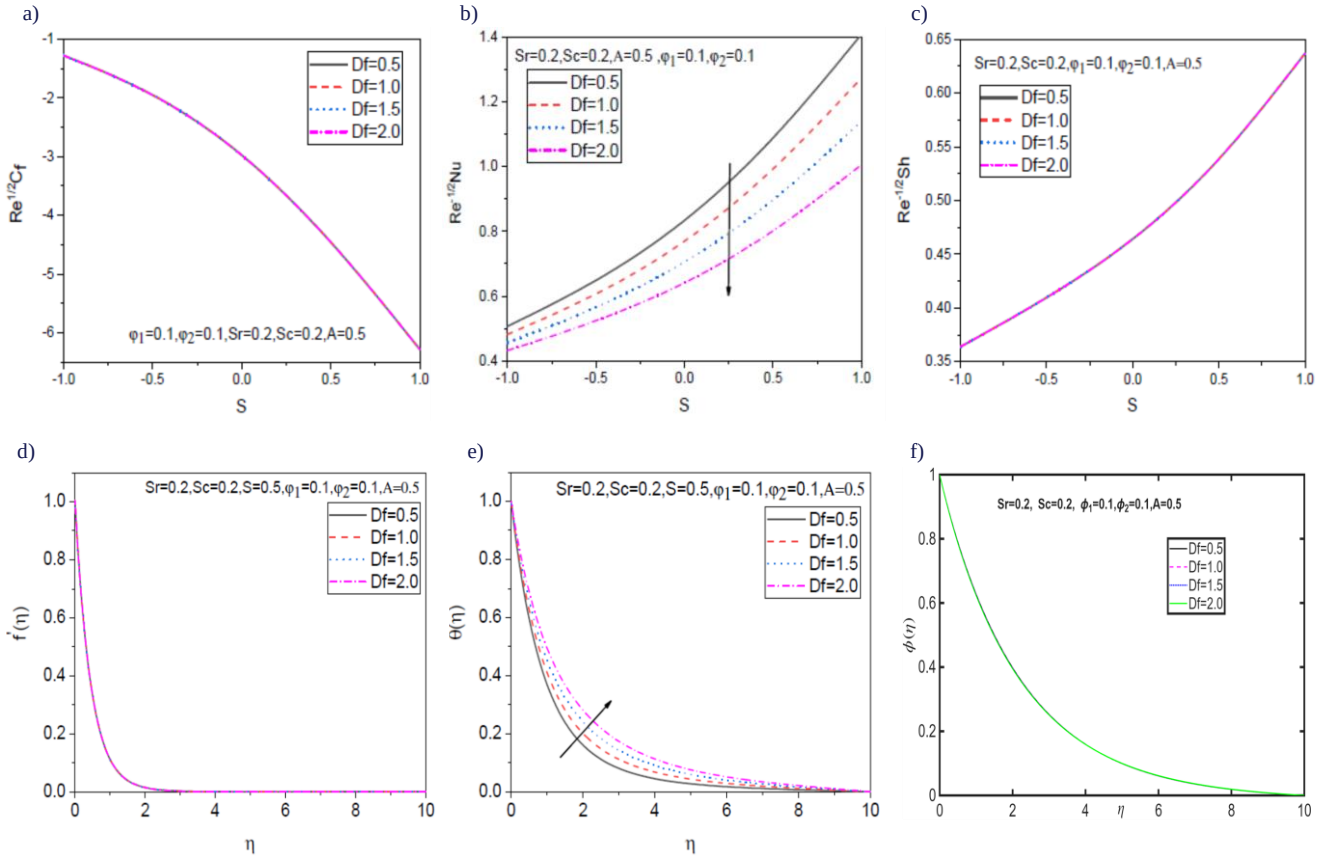

Fig. 7. Variation of $f''(0)$, $-\theta'(0)$, $-\phi'(0)$, $f'(\eta)$, $\theta(\eta)$ and $\phi(\eta)$ with Dufour parameter Df.

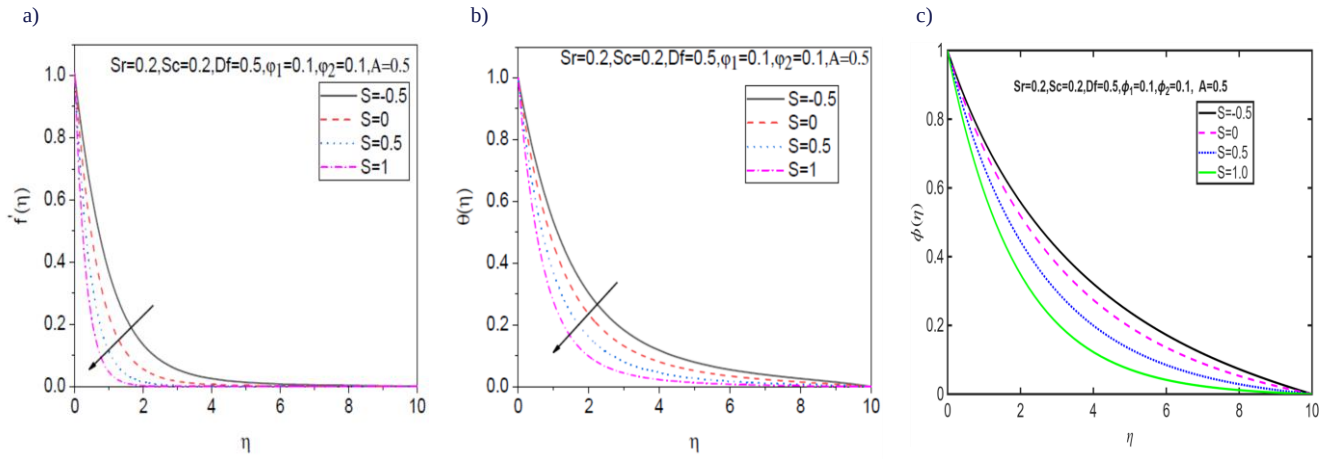

Fig. 8. Variation of $f'(\eta)$, $\theta(\eta)$ and $\phi(\eta)$ with suction/injection parameter S.

5. Conclusions

In this paper, the nonlinear differential equations arising from the hybrid nanofluid flow past a time-dependent sheet that is stretching radially with Dufour and Soret effects under the influence of the unsteadiness parameter A, suction or injection parameter, ϕ_1 and ϕ_2 at the surface, are solved employing the SLM approach. The effect of variables Sr, A, S, Sc, ϕ_1, ϕ_2 and Df over the pertinent physical quantities is scrutinised. The key findings are outlined below:

- The skin friction falls when the unsteadiness parameter ϕ_2 rises, and as ϕ_1 values rise, the skin friction enhances. As the Soret, Schmidt, and Dufour numbers rise, the skin friction doesn't alter.
- As the unsteadiness parameter increases, the Nusselt number rises, and decreases when ϕ_1 and ϕ_2 are increased. The Nusselt number diminishes as the Schmidt and Dufour numbers escalate but increases as the Soret number boosts.
- As ϕ_2 gets higher, the Sherwood number goes down and rises when the unsteadiness parameter ϕ_1 increases. The Sherwood number advances with the Schmidt number, but it stays constant while the Dufour number rises and falls with the Soret number.
- The velocity initially reduces and then increases when the unsteadiness parameter grows. The velocity decreases as the suction/injection parameter ϕ_2 increases, but the velocity escalates when ϕ_1 increases. As the Dufour, Schmidt, and Soret numbers grow, the velocity remains constant.
- The temperature decreases as the suction/injection parameter, Soret number, and unsteadiness parameter increase, and rises when ϕ_1, ϕ_2, and Dufour number are increased. The temperature increases initially and later diminishes while the Schmidt number grows.
- The concentration drops while the Schmidt number, unsteadiness parameter ϕ_1 and suction/injection parameter enhance, and rises when ϕ_2 and Soret number are increased. The rise in the Dufour number does not affects the concentration.

References

[1] Khan, M., Manzur, M., & ur Rahman, M. (2017). On axi-symmetric flow and heat transfer of Cross fluid over a radially stretching sheet. *Results in Physics*, 7, 3767−3772. doi: 10.1016/j.rinp.2017.08.039

[2] Ahmed, J., Shahzad, A, Begum, A., Ali, R, & Siddiqui, N. (2017). Effects of inclined Lorentz forces on boundary layer flow of Sisko fluid over a radially stretching sheet with radiative heat transfer. *Journal of the Brazilian Society of Mechanical Sciences and Engineering*, 39, 3039−3050. doi: 10.1007/s40430-017-0759-z

[3] Sreelakshmi, K., Sarojamma, G., & Josyula, R.M. (2018). Homotopy analysis of an unsteady flow heat transfer of a Jeffrey nanofluid over a radially stretching convective surface. *Journal of Nanofluids*, 7(1), 62−71. doi 10.1166/jon.2018.1432

[4] Khan, S.A., Nie, Y., & Ali, B. (2019). Multiple slip effects on magnetohydrodynamic axisymmetric buoyant nanofluid flow above a stretching sheet with radiation and chemical reaction. *Symmetry*, 11(9), 1171. doi: 10.3390/sym11091171

[5] Nayak, B, Mishra, S.R., & Krishna, G.G. (2019). Chemical reaction effect of an axisymmetric flow over radially stretched sheet. *Propulsion and Power Research*, 8(1), 79−84. doi: 10.1016/j.jppr.2019.01.002

[6] Shahzad, A., Ali, R., Hussain, M., & Kamran, M. (2017). Unsteady axisymmetric flow and heat transfer over time-dependent radially stretching sheet. *Alexandria Engineering Journal*, 56(1), 35−41. doi: 10.1016/j.aej.2016.08.030

[7] Shahzad, A., Gulistan, U., Ali, R., Iqbal, A., Benim, A.C., Kamran, M., Khan, S.U-D, Ud-Din Khan, S., & Farooq, A. (2020). Numerical study of axisymmetric flow and heat transfer in a liquid film over an unsteady radially stretching surface. *Mathematical Problems in Engineering*, 2020, 1−9. doi: 10.1155/2020/6737243

[8] Srinivasacharya, D., & Kumar, R.S. (2022) Artificial neural network modeling of the Casson fluid flow over unsteady radially stretching sheet with Soret and Dufour effects. *Journal of Thermal Analysis and Calorimetry*, 147(24), 14891−14903. doi: 10.1007/s10973-022-11694-w

[9] Chamkha, A.J., & Khaled. A.R.A. (2000). Similarity solution for hydromagnetic mixed convection heat and mass transfer for Hiemenz flow through porous media. *International Journal of Numerical Methods for Heat & Fluid Flow*, 10(1), 94–115. doi: 10.1108/09615530010306939

[10] Krishna, M.V., Anand, P.V.S., & Chamkha, A.J. (2019). Heat and mass transfer on free convective flow of a micropolar fluid through a porous surface with inclined magnetic field and Hall effects. *Special Topics & Reviews in Porous Media: An International Journal*, 10(3), 203−223. doi: 10.1615/SpecialTopicsRevPorousMedia.2018026943

[11] Krishna, M.V., Ahamad, A.N., & Chamkha. A.J. (2021). Hall and ion slip impacts on unsteady MHD convective rotating flow of heat generating/absorbing second grade fluid. *Alexandria Engineering Journal*, 60(1), 845−858. doi: 10.1016/j.aej.2020.10.013

[12] Choi, S.U.S., & Eastman, J.A. (1995). Enhancing thermal conductivity of fluids with nanoparticles. No. ANL/MSD/CP-84938; CONF-951135-29, *ASME International Engineering Congre & Expositon*, November 12−17, San Francisco, USA.

[13] Devi, S.A., & Devi, S.S.U. (2016). Numerical investigation of hydromagnetic hybrid Cu-Al_2O_3/water nanofluid flow over a permeable stretching sheet with suction. *International Journal of Nonlinear Sciences and Numerical Simulation*, 17(5), 249−257. doi: 10.1515/ijnsns-2016-0037

[14] Devi, S.U., & Devi, S.A. (2017). Heat transfer enhancement of Cu-Al_2O_3/water hybrid nanofluid flow over a stretching sheet. *Journal of the Nigerian Mathematical Society*, 36(2), 419−433.

[15] Hayat, T., & Nadeem, S. (2017). Heat transfer enhancement with Ag–CuO/water hybrid nanofluid. *Results in Physics*, 7, 2317−2324. doi: 10.1016/j.rinp.2017.06.034

[16] Yousefi, M., Dinarvand, S., Yazdi, M.E., & Pop, I. (2018). Stagnation-point flow of an aqueous titania-copper hybrid nanofluid toward a wavy cylinder. *International Journal of Numerical Methods for Heat and Fluid Flow*, 28(7), 1716−1735. doi: 10.1108/HFF-01-2018-0009

[17] Subhani, M., & Nadeem, S. (2019). Numerical analysis of micropolar hybrid nanofluid. *Applied Nanoscience*, 9(4), 447−459. doi: 10.1007/s13204-018-0926-2

[18] Ghadikolaei, S.S., Yassari, M., Sadeghi, H., Hosseinzadeh, K., & Ganji, D.D. (2017). Investigation on thermophysical properties of TiO_2-Cu/H_2O hybrid nanofluid transport dependent on shape factor in MHD stagnation point flow. *Powder Technology*, 322, 428−438. doi: 10.1016/j.powtec.2017.09.006

[19] Usman, M., Hamid, M., Zubair, T., Ul Haq, R., & Wang, W. (2018). Cu-Al_2O_3/water hybrid nanofluid through a permeable surface in the presence of nonlinear radiation and variable thermal conductivity via LSM. *International Journal of Heat and Mass Transfer*, 126, 1347−1356. doi: 10.1016/j.ijheatmasstransfer.2018.06.005

[20] Rostami, M.N., Dinarvand, S., & Pop, I. (2018). Dual solutions for mixed convective stagnation-point flow of an aqueous silica–alumina hybrid nanofluid. *Chinese Journal of Physics*, 56(5), 2465−2478. doi: 10.1016/j.cjph.2018.06.013

[21] Waini, I., Ishak, A., & Pop, I. (2019). Unsteady flow and heat transfer past a stretching/shrinking sheet in a hybrid nanofluid. *International Journal of Heat and Mass Transfer*, 136, 288−297. doi: 10.1016/j.ijheatmasstransfer.2019.02.101

[22] Waini, I., Ishak, A., & Pop, I. (2019). Hybrid nanofluid flow and heat transfer past a permeable stretching/shrinking surface with a convective boundary condition. In Journal of Physics: Conference Series, 1366(1), 012022. IOP Publishing. doi: 10.1088/1742-6596/1366/1/012022

[23] Gangadhar, K., Kumari, M.A. & Chamkha, A.J. EMHD Flow of Radiative Second-Grade Nanofluid over a Riga Plate due to Convective Heating: Revised Buongiorno's Nanofluid Model. *Arabian Journal for Science and Engineering*, 47(3), 8093–8103 (2022). doi: 10.1007/s13369-021-06092-7

[24] Ontela, S., Pattnaik, P.K., Panda, S., & Mishra, S.R. (2024). Optimizing heat transfer rate and sensitivity analysis of hybrid nanofluid flow over a radiating sheet: Applications in solar-powered charging stations. *Numerical Heat Transfer, Part B: Fundamentals*, 1–21. doi: 10.1080/10407790.2024.2341439

[25] Panda, S., Ontela, S., Pattnaik, P.K., & Mishra, S.R. (2024). Optimizing heat transfer rate with sensitivity analysis on nonlinear radiative hydromagnetic hybrid nanofluid flow considering catalytic effects and slip condition: Hamilton–Crosser and Yamada–Ota modelling. *Journal of Applied Mathematics and Mechanics (Zeitschrift fur Angewandte Mathematik und Mechanik)*, 104, e202301064. doi: 10.1002/zamm.202301064

[26] Pattnaik, P.K., Mishra, S.R., Thumma, T., Panda, S., & Ontela, S. (2024). Numerical investigation of radiative blood-based aluminum alloys nanofluid over a convective Riga sensor plate with the impact of diverse particle shape. *Journal of Thermal Analysis and Calorimetry*, 149, 2317–2329. doi: 10.1007/s10973-023-12820-y

[27] Panda, S., Ontela, S., Pattnaik, P.K., & Mishra, S.R., (2024). Radiating heat effect on Powell–Eyring blood-based hybrid nanofluid over a Riga plate with thermal stratification Cattaneo-Christov heat flux model, *Partial Differential Equations in Applied Mathematics*, 11, 100769. doi: 10.1016/j.padiff.2024.100769

[28] Nisar, K.S., Khan, U., Zaib, A., Khan, I. & Baleanu, D., (2020). Exploration of aluminum and titanium alloys in the stream-wise and secondary flow directions comprising the significant impacts of magnetohydrodynamic and hybrid nanofluid. *Crystals*, 10(8), 679. doi: 10.3390/cryst10080679

[29] Abad, J.M.N., Alizadeh, R., Fattahi, A., Doranehgard, M.H., Alhajri, E., & Karimi, N. (2020). Analysis of transport processes in a reacting flow of hybrid nanofluid around a bluff-body embedded in porous media using artificial neural network and particle swarm optimization. *Journal of Molecular Liquids*, 313, 113492. doi: 10.1016/j.molliq.2020.113492

[30] Hayat, T., Shehzad, S.A., & Alsaedi, A. (2012). Soret and Dufour effects on magnetohydrodynamic (MHD) flow of Casson fluid. *Applied Mathematics and Mechanics*, 33(10), 1301−1312. doi: 10.1007/s10483-012-1623-6

[31] Kameswaran, P.K., Shaw, S., & Sibanda, P. (2014). Dual solutions of Casson fluid flow over a stretching or shrinking sheet. *Sādhanā*, 39(6), 1573−1583. doi: 10.1007/s12046-014-0289-7

[32] Isa, S.S.P.M., Parvin, S., Arifin, N.M., Ali, F.M. & Ahmad, K. (2023). Soret-Dufour effects on the waterbased hybrid nanofluid flow with nanoparticles of Alumina and Copper. *Malaysian Journal of Mathematical Sciences*, 17(3), 283−304. doi: 10.47836/mjms.17.3.04

[33] Prathiba, A., Lakshmi, V.A., & Ramesh, V. (2023). A Computational Analysis of the Soret and Dufour Effects on a Rotating Hybrid Nanofluid. *Communications in Mathematics and Applications*, 14(2), 881. doi: 10.26713/cma.v14i2.2124

[34] Arif, U., Nawaz, M., & Salmi, A. (2022). Numerical study of simultaneous transport of heat and mass transfer in Maxwell hybrid nanofluid in the presence of Soret and Dufour effects. *Physica Scripta*, 97(2), 025207. doi: 10.1088/1402-4896/ac4d46

[35] Sharma, R.P., Gorai, D., & Das, K. (2022). Comparative study on hybrid nanofluid flow of Ag–CuO/H_2O over a curved stretching surface with Soret and Dufour effects. *Heat Transfer*, 51(7), 6365−6383. doi: 10.1002/htj.22595

[36] Vijay, N., & Sharma, K. (2023). Magnetohydrodynamic hybrid nanofluid flow over a decelerating rotating disk with Soret and Dufour effects. *Multidiscipline Modeling in Materials and Structures*, 19(2), 253−276. doi: 10.1108/MMMS-08-2022-0160

[37] Das, S.K., Choi, S.U., Yu, W. & Pradeep, T. (2007). *Nanofluids: Science and Technology*. John Wiley & Sons.

[38] Bachok, N., Ishak, A., & Pop, I. (2011). Flow and heat transfer over a rotating porous disk in a nanofluid, *Physica B: Condensed Matter*, 406(9), 1767–1772. doi: 10.1016/j.physb.2011.02.024

[39] Tassaddiq, A., Khan, S., Bilal, M., Gul, T., Mukhtar, S., Shah, Z., & Bonyah, E. (2020). Heat and mass transfer together with hybrid nanofluid flow over a rotating disk. *AIP Advances*, 10(5), 055317. doi: 10.1063/5.0010181

[40] Oztop, H.F., & Abu-Nada, E. (2008). Numerical study of natural convection in partially heated rectangular enclosures filled with nanofluids. *International Journal of Heat and Fluid Flow*, 29(5), 1326−1336. doi: 10.1016/j.ijheatfluidflow.2008.04.009